

DRIP: A Versatile Family of Space-Time ISAC Waveforms

Dexin Wang, Ahmad Bazzi, Marwa Chafii

Abstract—The following paper introduces Dual beam-similarity aware Integrated sensing and communications (ISAC) with controlled Peak-to-average power ratio (DRIP) waveforms. DRIP is a novel family of space-time ISAC waveforms designed for dynamic peak-to-average power ratio (PAPR) adjustment. The proposed DRIP waveforms are designed to conform to specified PAPR levels while exhibiting beampattern properties, effectively targeting multiple desired directions and suppressing interference for multi-target sensing applications, while closely resembling radar chirps. For communication purposes, the proposed DRIP waveforms aim to minimize multi-user interference across various constellations. Addressing the non-convexity of the optimization framework required for generating DRIP waveforms, we introduce a block cyclic coordinate descent algorithm. This iterative approach ensures convergence to an optimal ISAC waveform solution. Simulation results validate the DRIP waveforms' superior performance, versatility, and favorable ISAC trade-offs, highlighting their potential in advanced multi-target sensing and communication systems.

Index Terms—ISAC, DRIP, PAPR, space-time, waveform design, optimization

I. INTRODUCTION

The sixth generation (6G) of wireless communication standard is expected to represent a significant paradigm shift from its predecessors due to the numerous emerging applications [1], such as autonomous driving [2], unmanned aerial vehicles (UAVs) [3], industrial Internet-of-Things (IoT) [4]–[6], remote health monitoring, digital twins [7], and security [8], [9], with activities in the (sub-)terahertz spectrum [10] due to its ability to provide millimeter-level resolution and high-speed communication. The seamless integration of communication and sensing services, which are provided as distinct functionality in the current wireless standards, is a prerequisite for supporting these services [11], [12]. As a result, integrated sensing and communications (ISAC) has recently attracted a lot of interest as a 6G technology enabler [13], [14], due to its capability of improving spectral and energy efficiencies and to mutually benefit from both services [15]–[17]. According to [18], when sensing and communication (SAC) functions are used in tandem, they can benefit from one another mutually, but when they are used in competition, there is an inherent

trade-off. The superiority of an ISAC system over a frequency-division SAC system in terms of sensing communication rate region is demonstrated using a mutual-information framework in [19]. Very recently, the Technical Specification Group (TSG)-Service & System Aspects - Working Group 1 (SA1) of Third Generation Partnership Project (3GPP) have analysed a number of use cases for ISAC enabled by 5G systems, which include but are not limited to: human detection indoors and UAV detection outdoors, vehicle detection for advanced driver assistance systems (ADAS), rainfall monitoring and flooding, hand gesture recognition, public safety, and more [20].

Indeed, ISAC systems can simultaneously perform communication and radar tasks by designing and transmitting a single waveform via a fully-shared transceiver. This leads to efficient resource utilization [21] with lower system cost and lower power consumption. Hence, advanced designs for dual-functional waveforms are essential to reconcile the conflicting demands of communication and sensing, while also leveraging integration and coordination benefits. Even more, additional sophistication arises when it becomes necessary to constrain the peak-to-average power ratio (PAPR) of the ISAC signal under a specified threshold, due to radio frequency (RF) limitations. Specifically, maintaining low PAPR transmissions becomes crucial, when nonlinear high power amplifiers (HPAs) are part of the RF frontend of the transmit chain [22]. In principle, low PAPR waveforms are desired, as it enables us to tune the HPA's quiescent point as close as possible to the optimal operating point, limiting the impact of clipping. Certainly, extensive research has been conducted on methods for reducing PAPR. For instance, [23] establishes essential conditions for waveforms with superior PAPR compared to orthogonal frequency-division multiplexing (OFDM), while [24] introduces PAPR reduction techniques tailored for OFDM. In addition, [25] employs convex optimization techniques to synthesize sequences that exhibit favorable properties of low PAPR, while adhering to spectral mask constraints. Despite research efforts on PAPR reduction and optimization, ISAC waveforms should be pragmatically dealt with when considering PAPR control due to their dual nature and the conflicting nature of the SAC information within the waveform.

A. Existing Work

In [26], the authors look into joint scheduling and beamforming for ISAC-enabled systems under ultra reliable and low latency communications (URLLC) requirements, whereby a joint scheduling and beamforming framework is proposed for joint data transmission and environment sensing. In [27],

Dexin Wang is with the NYU Tandon School of Engineering, Brooklyn, 11201, NY, US and the Engineering Division, New York University (NYU) Abu Dhabi, 129188, UAE (email: dw2712@nyu.edu).

Ahmad Bazzi and Marwa Chafii are with Engineering Division, New York University (NYU) Abu Dhabi, 129188, UAE and NYU WIRELESS, NYU Tandon School of Engineering, Brooklyn, 11201, NY, USA (email: ahmad.bazzi@nyu.edu, marwa.chafii@nyu.edu).

Manuscript received xxx

the authors first derive the expression for Cramér-Rao bound (CRB) of angle of arrival (AoA) and distance estimate for sensing multiple wideband sources, and then minimize that while guaranteeing a communication quality-of-service for each downlink user assuming a near-field channel model. Moreover, in [28], the authors design a method for designing waveforms in cooperative joint radar-communications systems, which takes into account the age-of-information (AoI). More specifically, the framework maximizes the radar mutual information under AoI performance and communication data rate to optimize for the allocated power of the OFDM signal. [29] also uses OFDM for ISAC waveform design to suppress multi-tone narrowband interference via an optimization framework that trades off between data rate for communications and peak sidelobe levels for sensing. The work in [30] proposes a beamspace waveform design and beam selection problem for ISAC systems equipped with lens antenna arrays (LAAs), whereby the goal is to consume minimum system power, under SAC constraints. Furthermore, a low probability of intercept (LPI) ISAC waveform design was proposed in [31] for radar systems to jointly attain a low LPI for radar functionality and the ability to maintain communication with radar nodes. Nevertheless, a waveform design approach was proposed in [32] for bistatic dual-functional radar and communication (DFRC) taking into account CRB for AoA and angle of departure (AoD) along with the symbol error rate for communications. Moreover, the work in [33] uses the concept of mutual information (MI) for both SAC services to conduct ISAC waveform design dedicated to multicarrier systems. The methodology in [34] uses orthogonal time frequency space (OTFS) signaling for delay-doppler spectrum estimation, whereby an amplitude barycenter calibration method is designed to yield good sensing performance for fixed communication bandwidth and frame duration. Within the same context, the work in [35] designs a receiver window for OTFS signaling in ISAC systems and develops a barycenter calibration method that considers high-order spectra of channels in the delay-doppler domain. Also, [36] uses OTFS to jointly design an ISAC signal by optimizing the ambiguity function's weighted integrated sidelobe level, under signal-to-noise ratio constraint. Furthermore, the work in [37] studies ISAC waveform design for communication-centric systems targeted to maximize energy efficiency, under CRB guarantees for target detection and signal to interference plus noise ratio (SINR) guarantees for communication. The works in [38], [39] consider ISAC waveform design with the aid of reconfigurable intelligent surface (RIS). In particular, the authors in [38] consider secure waveform design with the help of RIS, where an ISAC base station communicates with multiple users in the presence of an eavesdropper. The work in [40] uses simultaneously transmitting and reflecting surface (STARS), whereby sensors are placed at STARS to address the significant path loss of sensing. In particular, the 2D CRB for joint AoA and AoD was minimized under a communication requirement. *Unlike existing methods, we generate low-PAPR space-time ISAC waveforms for multi-target sensing waveforms that maintain radar characteristics while enabling effective communication. Additionally, we prove that, thanks to our proposed method, it is always guaranteed to converge*

to a stable waveform that is optimized for multi-user (MU) communications and multi-target sensing while minimizing interferers, produced through reflection from objects that are not the targets of interest, such as clutter.

B. Contributions and Insights

This work derives a family of space-time ISAC waveform design adhering to desired PAPR levels. In particular, a DFRC base station (BS) intends to communicate with downlink (DL) users, while sensing multiple targets through the received backscattered signal of the same transmitted ISAC signal, which is to be designed. We first formulate an optimization framework that enables us to generate a family of space-time ISAC waveforms dedicated for the aforementioned tasks and constraints. We then design a block cyclic coordinate descent (BCCD) method intended to generate such ISAC waveforms. To that purpose, we have summarized our contributions below.

- **Space-time controlled PAPR ISAC waveform design.** Due to the random nature of communication waveforms, which typically results in degraded sensing performance due to several factors, such as a high PAPR and random autocorrelation properties, a fundamental contribution of this work is to design space-time ISAC waveform conveying random communication information, with a closeness to a given radar waveform, hence preserving the radar autocorrelation features. Moreover, the proposed ISAC waveforms are capable to simultaneously steer/beam towards intended directions, while rejecting interfering directions, deeming them suitable for *multi-target sensing* applications. In addition, the PAPR of the proposed ISAC waveforms can be controlled to generate low-PAPR waveforms, which is yet another desirable feature in future systems. An optimization framework is derived to accommodate the aforementioned ISAC features.
- **Optimization method to generate space-time ISAC waveforms.** As the proposed optimization framework is non-convex by nature, we propose an iterative BCCD algorithm that can be readily used to generate the described space-time ISAC waveforms.
- **Convergence Analysis.** We provide a rigorous convergence analysis for the proposed BCCD algorithm for space-time ISAC waveform generation. Specifically, by adopting tools from numerical optimization, it is revealed that the proposed space-time ISAC waveform design method is always guaranteed to converge to a stable waveform, despite the stringent sensing and PAPR constraints included in the proposed optimization problem.
- **Extensive simulation results.** Extensive simulation results are provided to compare the performance of the proposed ISAC waveform design method with various benchmark schemes, in terms of average sum rate while trading off the similarity rate, which demonstrates the great potential of our proposed method for ISAC systems under a controllable PAPR constraint. Moreover, we also reveal convergence performances of the various ISAC metrics included, i.e. the average radar SINR and multi-user interference (MUI), in addition to the PAPR statistics

and the various ISAC tradeoffs that can be expected by adopting the proposed framework.

Furthermore, we unveil some important insights, i.e.

- Simulations reveal that the proposed BCCD algorithm requires few iterations to converge towards a Dual beam-similarity aware Integrated sensing and communications with controlled Peak-to-average power ratio (DRIP) waveform.
- A similarity-rate tradeoff exists for DRIP-type waveforms. In particular, for a very demanding stringent similarity constraint, an average sum rate of about 1.25 bps/Hz is achieved, whereby relaxing similarity can boost the average sum rate to as high as 6 bps/Hz.
- The analysis of DRIP beampatterns¹ reveals that increasing similarity to a radar chirp improves sidelobe performance but results in ambiguous beam peaks. When the radar chirp similarity decreases, DRIP waveforms produce sharper peaks directed at targets, enhancing beamforming applications. Notably, targets further away achieve clearer peaks even at lower similarity rate values. For instance, one scenario shows distinct peaks of 48 dB and 43 dB, while another scenario shows an ambiguous plateau around 37 dB as soon as targets become closer, which is related to the spatial resolution of DRIP.

C. Organization and Notations

The following paper is organized as follows: Section II introduces the considered ISAC model of MU-communications and multiple targets. After introducing the appropriate ISAC metrics involved in this work, we present the dual beam-similarity aware ISAC optimization with PAPR control optimization framework in Section III. In Section IV, we tailor a DFRC waveform design algorithm via block cyclic coordinate descent, followed by a detailed convergence analysis in Section V. In Section VI, simulation results are provided to evaluate the performance of the proposed ISAC waveform design method. Finally, we conclude the paper in Section VII.

Notation: Upper-case and lower-case boldface letters denote matrices and vectors, respectively. $(\cdot)^T$, $(\cdot)^*$ and $(\cdot)^H$ represent the transpose, the conjugate and the transpose-conjugate operators, respectively. The statistical expectation is denoted as $\mathbb{E}\{\cdot\}$. For any complex number $z \in \mathbb{C}$, the magnitude is denoted as $|z|$, and its angle is $\angle z$. The ℓ_2 norm of a vector \mathbf{x} is denoted as $\|\mathbf{x}\|$. The matrix \mathbf{I}_N is the identity matrix of size $N \times N$. The zero-vector is $\mathbf{0}$. For matrix indexing, the $(i, j)^{th}$ entry of matrix \mathbf{A} is denoted by $[\mathbf{A}]_{i,j}$ and its j^{th} column is denoted as $[\mathbf{A}]_{:,j}$. The $[x]^+$ operator returns the maximum between x and 0. A positive semi-definite matrix is denoted as $\mathbf{A} \succeq \mathbf{0}$ and a vector \mathbf{x} with all non-negative entries is denoted as $\mathbf{x} \succeq \mathbf{0}$. The all-ones vector of appropriate dimensions is denoted by $\mathbf{1}$. The vectorization operator is denoted as vec .

II. SYSTEM MODEL

Let us assume that a DFRC BS, supporting a co-located mono-static unit of N_T transmit antennas and N_R receive

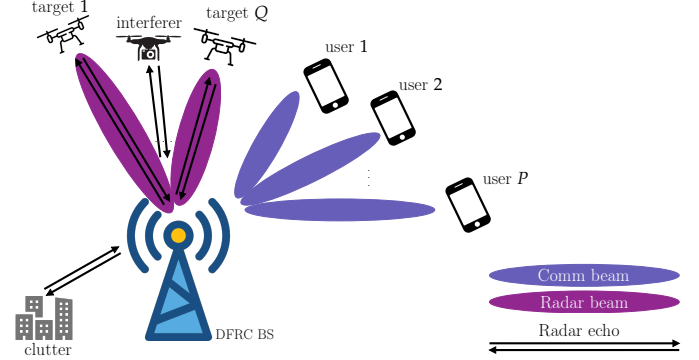


Fig. 1. An ISAC scenario composed of P users for MU-communications and Q multiple targets in the presence of I interferers.

antennas, is to support MU communications toward K DL communication single-antenna users, while sensing Q targets² in the vicinity, in the presence of I interfering targets, which can also be classified as clutter. Moreover, the radar targets of interest are assumed to be positioned at $\theta_1 \dots \theta_Q$, representing the angles of arrival (AoAs) relative to the DFRC BS, whereas the interfering targets are assumed to be located at $\bar{\theta}_1 \dots \bar{\theta}_I$. An illustration is given in Fig. 1.

A. Radar Backscattered Model

Since we assume a mono-static configuration at the DFRC BS, the AoD and AoA of the different backscattering components are essentially identical. To this extent, we can write

$$\mathbf{Y}_r = \sum_{q=1}^Q \gamma_q \mathbf{\Pi}(\theta_q) \mathbf{X} + \sum_{i=1}^I \tilde{\gamma}_i \mathbf{\Pi}(\bar{\theta}_i) \mathbf{X} + \mathbf{Z}_r, \quad (1)$$

where $\mathbf{Y}_r \in \mathbb{C}^{N_R \times L}$ is the received backscattered echo. In addition, γ_q represents the two-way complex channel coefficient between the DFRC BS and the q^{th} radar target of interest, which is proportional to the radar cross-section (RCS) of the targets. In addition, $\tilde{\gamma}_i$ is the two-way channel coefficient between the DFRC and the i^{th} interferer. Note that the clutter can be accommodated within the interfering terms. Referring to (5), we have that $\mathbf{\Pi}(\theta) = \mathbf{a}_{N_R}(\theta) \mathbf{a}_{N_T}^T(\theta)$, where $\mathbf{a}_{N_T}(\theta) \in \mathbb{C}^{N_T \times 1}$ and $\mathbf{a}_{N_R}(\theta) \in \mathbb{C}^{N_R \times 1}$ denote the transmitting and receiving array steering vectors at angle θ , respectively. For example, if the antenna array follows a uniform linear antenna (ULA) setting, then the steering vectors of transmit and receive arrays can be expressed as

$$\mathbf{a}_{N_T}(\theta) = [1 \quad e^{j \frac{2\pi}{\lambda} d_T \sin(\theta)} \quad \dots \quad e^{j \frac{2\pi}{\lambda} d_T (N_T-1) \sin(\theta)}]^T, \quad (2)$$

$$\mathbf{a}_{N_R}(\theta) = [1 \quad e^{j \frac{2\pi}{\lambda} d_R \sin(\theta)} \quad \dots \quad e^{j \frac{2\pi}{\lambda} d_R (N_R-1) \sin(\theta)}]^T, \quad (3)$$

respectively. Note that in (2) and (3), λ is the wavelength; whereas, the inter-element spacing of transmit and receive arrays are denoted as d_T and d_R , respectively. Moreover, the noise of the radar sub-system is independent and identically distributed (i.i.d) Gaussian random variables modeled

¹The resulting beampatterns obtained by the DRIP waveforms.

²The targets do not have any transceiver capability.

as $\mathbf{Z}_r \sim \mathcal{CN}(0, \sigma_r^2 \mathbf{I}_N)$. In contrast to our previous approach [41], we hereby aim to design a controlled PAPR space-time ISAC waveform $\mathbf{X} \in \mathbb{C}^{N_T \times L}$, under joint multi-target radar beamforming and similarity with respect to a chirp with desirable auto-correlation properties. Therefore, this article offers a sophisticated capability of focusing the PAPR-controlled chirp energy towards multiple targets (instead of broadcasting it), in addition to rejecting interfering sources, while performing MU-communications. As shown in the next subsection, the same waveform \mathbf{X} is used for MU communication tasks.

B. Multi-user Communication Model

A transmission of an ISAC signal over N_T antennas and sampled at L time instances, i.e. \mathbf{X} , in the DL communication sense is initiated from a DFRC BS over a slow-fading block Rayleigh fading communication channel, say $\mathbf{H} = [\mathbf{h}_1 \ \mathbf{h}_2 \ \dots \ \mathbf{h}_P]^T \in \mathbb{C}^{P \times N_T}$. The DFRC BS aims at conveying a constellation $\mathbf{S} \in \mathbb{C}^{P \times L}$, e.g. quadrature amplitude modulation (QAM) or phase-shift keying (PSK), towards P users. Assuming the channel to be constant over the transmission period, one can write the received signal as

$$\mathbf{Y}_c = \mathbf{H}\mathbf{X} + \mathbf{Z}_c, \quad (4)$$

where $\mathbf{Y}_c \in \mathbb{C}^{P \times L}$ is the matrix of received signals, and the p^{th} row of \mathbf{Y}_c contains the waveform intended to user p . The number of time samples of the DFRC BS signal is L . Furthermore, the background noise assumed to be additive white Gaussian noise (AWGN) is zero mean and a scaled multiple of identity covariance matrix, is denoted as $\mathbf{Z}_c \in \mathbb{C}^{P \times L}$, where $\text{vec}(\mathbf{Z}_c) \sim \mathcal{CN}(0, \sigma_c^2 \mathbf{I}_{KL})$. Here, σ_c^2 represents the communication noise variance power.

C. ISAC Metrics

Before designing a space-time ISAC waveform optimization problem dedicated for dual beam illumination and similarity chirp rate with a controllable PAPR, a key element is to define metrics relevant to the waveform design problem in consideration. In this paper, we consider two key metrics for radar for space-time design.

a) *Radar chirp similarity*: The first metric is the similarity constraint with a desired radar chirping signal. Denoting the desired radar signal as $\mathbf{X}_0 \in \mathbb{C}^{N_T \times L}$, the similarity constraint can be formed through a sphere centered at the reference radar signal \mathbf{X}_0 with a radius ϵ , namely $\mathbf{x} \in \mathcal{B}_\epsilon(\mathbf{x}_0)$, where $\mathcal{B}_\epsilon(\mathbf{x}_0) = \{\mathbf{x}, \|\mathbf{x} - \mathbf{x}_0\|^2 \leq \epsilon^2\}$, $\mathbf{x} = \text{vec}(\mathbf{X})$ and $\mathbf{x}_0 = \text{vec}(\mathbf{X}_0)$.

b) *Radar SINR*: Moreover, for space-time beamforming, we define $\mathbf{u}_{q,\ell}$ as the beamforming vector intended for the q^{th} target and the ℓ^{th} time instance, i.e. the received signal in (5) is combined as

$$\begin{aligned} \mathbf{u}_{q,\ell}^H [\mathbf{Y}_r]_{:, \ell} &= \gamma_q \mathbf{u}_{q,\ell}^H \mathbf{\Pi}(\theta_q) \mathbf{X}_{:, \ell} + \sum_{q' \neq q} \gamma_{q'} \mathbf{u}_{q,\ell}^H \mathbf{\Pi}(\theta_{q'}) \mathbf{X}_{:, \ell} \\ &+ \sum_{i=1}^I \bar{\gamma}_i \mathbf{u}_{q,\ell}^H \mathbf{\Pi}(\theta_i) \mathbf{X}_{:, \ell} + \mathbf{u}_{q,\ell}^H [\mathbf{Z}_r]_{:, \ell}, \end{aligned} \quad (5)$$

The first term contains the target of interest, i.e. q^{th} target. The second term contains inter-target interference and the third

term contains interference from interfering targets/clutter and the last term is radar noise. To this end, we can define the radar SINR associated with the q^{th} target in (6), at the bottom of the next page, where $\sigma_q^2 = \mathbb{E}(|\gamma_q|^2)$ and $\bar{\sigma}_i^2 = \mathbb{E}(|\bar{\gamma}_i|^2)$.

c) *Peak-to-average power ratio*: The PAPR is a waveform measure that reflects the waveform's peak values to its average power. For instance, a constant magnitude waveform exhibits a unit PAPR, which is the minimal PAPR a waveform can have. Mathematically, the PAPR of a signal vector \mathbf{x} with $N_T L$ complex-valued samples can be defined as

$$\text{PAPR}(\mathbf{x}) = \frac{\max_{\ell=1 \dots N_T L} |\mathbf{x}(\ell)|^2}{\frac{1}{L} \sum_{\ell=1}^{N_T L} |\mathbf{x}(\ell)|^2}. \quad (7)$$

where $\mathbf{x} = \text{vec}(\mathbf{X})$.

d) *MU interference for communications*: Based on (4), we can re-write the received signal just by adding and subtracting the desired signal carrying information symbols $\mathbf{S} \in \mathbb{C}^{P \times L}$ as

$$\mathbf{Y}_c = \mathbf{S} + \mathbf{H}\mathbf{X} - \mathbf{S} + \mathbf{Z}_c. \quad (8)$$

Under a fixed transmit constellation energy, minimizing the total energy within the MU interference contributes to maximizing the achievable sum-rate of all communication users [42]. In essence, the total MU interference energy is given as

$$E_{\text{MUI}} = \|\mathbf{H}\mathbf{X} - \mathbf{S}\|_F^2. \quad (9)$$

In the next section, we introduce an optimization framework dedicated to generate space-time ISAC waveforms that are capable of adhering to a given PAPR, while performing communication and space-time sensing tasks.

III. DUAL BEAM-SIMILARITY AWARE ISAC OPTIMIZATION WITH PAPR CONTROL

Now, we introduce our optimization framework that takes into account multiple metrics related to sensing, communication and PAPR restrictions. Relevant to sensing, we target a given similarity rate relative to a given chirp \mathbf{x}_0 , which is controlled via a given level, i.e. ϵ . Also, for sensing design, we allude to the significance of highlighting radar beams toward multiple targets, while simultaneously minimizing the impact of interfering sources within the scene. In particular, this capability is translated into a minimum guarantee, captured by \bar{g}_q , on the radar SINR for each prospective target. As for the MU communication counterpart, we aim at minimizing the MU interference, which is directly related to maximizing the sum rate of the communication users [42].

Since one of our tasks is also to generate waveforms under a desired PAPR value, the PAPR on the waveform \mathbf{X} is restricted to be upper-bounded by a given level, say η . To this end, our DRIP optimization problem can be formulated as follows

$$(\mathcal{P}_{\text{DRIP}}) : \begin{cases} \min_{\mathbf{X}, \mathbf{U}} & \|\mathbf{H}\mathbf{X} - \mathbf{S}\|^2 \\ \text{s.t.} & \text{PAPR}(\mathbf{x}) \leq \eta, \\ & \mathbf{x} \in \mathcal{B}_\epsilon(\mathbf{x}_0), \\ & g_q \geq \bar{g}_q, \quad \forall q, \end{cases} \quad (10)$$

where $\mathbf{U} = [\mathbf{u}_{1,1} \dots \mathbf{u}_{1,L} \dots \mathbf{u}_{Q,1} \dots \mathbf{u}_{Q,L}]$ contains all beamforming vectors, and $\mathbf{x} = \text{vec}(\mathbf{X})$. Imposing a power budget constraint on the transmit waveforms, a total unit norm on \mathbf{X} is taken into account via a norm constraint, i.e. $\|\mathbf{x}\|^2 = 1$. The equivalent DRIP optimization problem in consideration is

$$(\mathcal{P}_{\text{DRIP}}) : \begin{cases} \min_{\mathbf{x}, \mathbf{U}} & \|\mathbf{H}\mathbf{X} - \mathbf{S}\|^2 \\ \text{s.t.} & \|\mathbf{x}\|^2 = 1, \quad \mathbf{x}^H \mathbf{F}_p \mathbf{x} \leq \frac{\eta}{N_T L}, \quad \forall p, \\ & \mathbf{x} \in \mathcal{B}_\epsilon(\mathbf{x}_0), \\ & g_q \geq \bar{g}_q, \quad \forall q, \end{cases} \quad (11)$$

where \mathbf{F}_p is an all-zeros matrix, except for 1 positioned at the p^{th} diagonal component. Before we proceed, we upper bound the MU interference energy as follows

$$\begin{aligned} \|\mathbf{H}\mathbf{X} - \mathbf{S}\|_F^2 &= \|\mathbf{H}(\mathbf{X} - \mathbf{H}^H(\mathbf{H}\mathbf{H}^H)^{-1}\mathbf{S})\|_F^2 \\ &\leq \|\mathbf{H}\|_F^2 \|\mathbf{x} - \mathbf{x}_{\text{comm}}\|^2, \end{aligned} \quad (12)$$

where we invoked $\|\mathbf{A}\mathbf{B}\|_F^2 \leq \|\mathbf{A}\|_F^2 \|\mathbf{B}\|_F^2$ and $\mathbf{x}_{\text{comm}} = \text{vec}(\mathbf{H}^H(\mathbf{H}\mathbf{H}^H)^{-1}\mathbf{S})$. Therefore, we replace the objective function in (11) with its upper bound in (12), resulting in a relaxed version of $(\mathcal{P}_{\text{DRIP}})$ as given below

$$(\tilde{\mathcal{P}}_{\text{DRIP}}) : \begin{cases} \min_{\mathbf{x}, \mathbf{U}} & \|\mathbf{x} - \mathbf{x}_{\text{comm}}\|^2 \\ \text{s.t.} & \|\mathbf{x}\|^2 = 1, \quad \mathbf{x}^H \mathbf{F}_p \mathbf{x} \leq \frac{\eta}{N_T L}, \quad \forall p, \\ & \mathbf{x} \in \mathcal{B}_\epsilon(\mathbf{x}_0), \\ & g_q \geq \bar{g}_q, \quad \forall q. \end{cases} \quad (13)$$

It is worth expressing a fundamental difference between the introduced DRIP design and our previously proposed Similarity aware Integrated sensing and communications with tunable Peak-to-average power ratio (SRIP) approach in [41]. SRIP operates over the temporal dimension only, which is ideal for single-antenna ISAC systems as the optimization is done solely over time domain. In contrast, DRIP is intended for a joint space-time ISAC waveforms, whereby space and time resources are jointly taken into account to yield an ISAC waveform with a desired PAPR level. More specifically, the space-time ISAC waveform generated by DRIP not only preserves a similarity with respect to a radar waveform, while reducing MUI for communication and maintaining a desirable PAPR level, but is also capable of steering its energy towards multiple directions simultaneously to sense radar targets of interest, while rejecting interference and clutter along given directions, with the aid of receive beamforming. It should now be clear that problem $(\mathcal{P}_{\text{DRIP}})$ in (10), or its relaxed counterpart in (13), represent a family of waveforms. In particular, for a given $(\epsilon, \eta, \{\bar{g}_q\}, \mathbf{H}, \mathbf{S})$, a DRIP waveform \mathbf{X} along with its receive beamformers \mathbf{U} are to be generated. Due to the non-convexity of $\tilde{\mathcal{P}}_{\text{DRIP}}$ in (13), in the next section, we

design a suitable algorithm dedicated to generate DRIP-type waveforms.

IV. DRIP WAVEFORMS VIA BLOCK CYCLIC COORDINATE DESCENT

The first block of the BCCD method optimizes with respect to \mathbf{U} . Before we proceed, note that the SINR in (6) can be written in the form of a generalized Rayleigh quotient term as

$$g_q = \frac{\mathbf{u}_q^H \mathbf{T}_q^1 \mathbf{u}_q}{\mathbf{u}_q^H \mathbf{T}_q^2 \mathbf{u}_q}, \quad (14)$$

where

$$\begin{aligned} \mathbf{T}_{1,q} &= \sigma_q^2 (\mathbf{I}_L \otimes \mathbf{\Pi}(\theta_q)) \mathbf{x} \mathbf{x}^H (\mathbf{I}_L \otimes \mathbf{\Pi}(\theta_q))^H, \\ \mathbf{T}_{2,q} &= \sum_{q' \neq q} \sigma_{q'}^2 (\mathbf{I}_L \otimes \mathbf{\Pi}(\theta_{q'})) \mathbf{x} \mathbf{x}^H (\mathbf{I}_L \otimes \mathbf{\Pi}(\theta_{q'}))^H \\ &\quad + \sum_i \bar{\sigma}_i^2 (\mathbf{I}_L \otimes \mathbf{\Pi}(\bar{\theta}_i)) \mathbf{x} \mathbf{x}^H (\mathbf{I}_L \otimes \mathbf{\Pi}(\bar{\theta}_i))^H + \sigma_r^2 \mathbf{I}, \end{aligned}$$

and $\mathbf{u}_q = [\mathbf{u}_{q,1}^T \dots \mathbf{u}_{q,L}^T]^T$. Next, observe that the only quantity depending on \mathbf{u}_q is g_q . So, adopting an alternating optimization approach, fixing \mathbf{x} , the optimization problem in (13) should aim at maximizing g_q . To this extent, we have the following Q independent optimization problems to be solved

$$\hat{\mathbf{u}}_q = \arg \max_{\mathbf{u}_q} \frac{\mathbf{u}_q^H \mathbf{T}_{1,q} \mathbf{u}_q}{\mathbf{u}_q^H \mathbf{T}_{2,q} \mathbf{u}_q}, \quad \forall q = 1 \dots Q. \quad (15)$$

Due to the fractional nature of the maximization in (15), a possible workaround is by holding the numerator constant, and minimizing the denominator, namely

$$(\tilde{\mathcal{P}}_{\text{DRIP}}^u) : \begin{cases} \min_{\mathbf{u}_q} & \mathbf{u}_q^H \mathbf{T}_{2,q} \mathbf{u}_q \\ \text{s.t.} & \mathbf{u}_q^H (\mathbf{I}_L \otimes \mathbf{\Pi}(\theta_q)) \mathbf{x} = \zeta, \end{cases} \quad (16)$$

where ζ is a constant. Using optimization theory, the solution of $(\tilde{\mathcal{P}}_{\text{DRIP}}^u)$ in (16) above is given as

$$\hat{\mathbf{u}}_q = \frac{\mathbf{T}_{2,q}^{-1} (\mathbf{I}_L \otimes \mathbf{\Pi}(\theta_q)) \mathbf{x}}{\mathbf{x}^H (\mathbf{I}_L \otimes \mathbf{\Pi}(\theta_q))^H \mathbf{T}_{2,q}^{-1} (\mathbf{I}_L \otimes \mathbf{\Pi}(\theta_q)) \mathbf{x}} \quad (17)$$

After obtaining $\hat{\mathbf{u}}_q$, the radar SINR is evaluated at this point, and hence the problem in (13) becomes

$$(\tilde{\mathcal{P}}_{\text{DRIP}}^x) : \begin{cases} \min_{\mathbf{x}} & \|\mathbf{x} - \mathbf{x}_{\text{comm}}\|^2 \\ \text{s.t.} & \|\mathbf{x}\|^2 = 1, \quad \mathbf{x}^H \mathbf{F}_p \mathbf{x} \leq \frac{\eta}{N_T L}, \quad \forall p \\ & \mathbf{x} \in \mathcal{B}_\epsilon(\mathbf{x}_0), \quad \hat{g}_q \geq \bar{g}_q, \quad \forall q, \end{cases} \quad (18)$$

where $\hat{g}_q = \frac{\hat{\mathbf{u}}_q^H \mathbf{T}_{1,q} \hat{\mathbf{u}}_q}{\hat{\mathbf{u}}_q^H \mathbf{T}_{2,q} \hat{\mathbf{u}}_q}$, $\forall q = 1 \dots Q$. Now, we introduce the following property

$$g_q = \frac{\sigma_q^2 \sum_{\ell=1}^L \|\mathbf{u}_{q,\ell}^H \mathbf{\Pi}(\theta_q) \mathbf{X}_{:, \ell}\|^2}{\sum_{\ell=1}^L \left(\sum_{q' \neq q}^Q \sigma_{q'}^2 \|\mathbf{u}_{q,\ell}^H \mathbf{\Pi}(\theta_{q'}) \mathbf{X}_{:, \ell}\|^2 + \sum_{i=1}^I \bar{\sigma}_i^2 \|\mathbf{u}_{q,\ell}^H \mathbf{\Pi}(\bar{\theta}_i) \mathbf{X}_{:, \ell}\|^2 + \sigma_r^2 \|\mathbf{u}_{q,\ell}\|^2 \right)} \quad (6)$$

Property 1: Problem $(\widetilde{\mathcal{P}}_{\text{DRIP}}^x)$ in (18) is a quadratic constrained quadratic programming (QCQP) optimization problem with $N_T L + Q + 3$ inequality quadratic constraints and no equality constraints, i.e.

$$(\mathcal{S}_{\text{QCQP}}) : \begin{cases} \min_{\mathbf{x}_r} & \mathbf{x}_r^T \mathbf{P}_0 \mathbf{x}_r + \mathbf{q}_0^T \mathbf{x}_r \\ \text{s.t.} & \mathbf{x}_r^T \mathbf{P}_i \mathbf{x}_r + \mathbf{q}_i^T \mathbf{x}_r \leq r_i, \quad \forall i = 1 \dots m. \end{cases} \quad (19)$$

where $m = N_T L + Q + 3$. The optimization variable is real-valued $\mathbf{x}_r \in \mathbb{R}^{2N_T L \times 1}$. In addition, $\mathbf{P}_i \in \mathbb{R}^{2N_T L \times 2N_T L}$, $\mathbf{q}_i \in \mathbb{R}^{2N_T L \times 1}$, and $r_i \in \mathbb{R}$ for all i .

Proof: See Appendix A.

Next, we apply non-negative slack variables onto the inequality constraints so that the inequalities are expressed as linear instead of quadratic. Therefore, problem $(\mathcal{S}_{\text{QCQP}})$ can be equivalently represented by the following

$$(\mathcal{S}'_{\text{QCQP}}) : \begin{cases} \min_{\mathbf{x}_r} & \mathbf{x}_r^T \mathbf{P}_0 \mathbf{x}_r + \mathbf{q}_0^T \mathbf{x}_r \\ \text{s.t.} & \mathbf{x}_r^T \mathbf{P}_i \mathbf{x}_r + \mathbf{q}_i^T \mathbf{x}_r + \varphi_i = r_i, \quad \forall i = 1 \dots m, \\ & \varphi_i \geq 0, \quad \forall i = 1 \dots m. \end{cases} \quad (20)$$

Stacking the slack variables in a vector, say $\boldsymbol{\varphi} = [\varphi_1 \dots \varphi_m]^T$, the augmented Lagrangian associated with the problem in (20) is given as

$$\begin{aligned} \mathcal{L}_\rho(\mathbf{x}_r, \boldsymbol{\varphi}, \boldsymbol{\lambda}) &= \mathbf{x}_r^T \mathbf{P}_0 \mathbf{x}_r + \mathbf{q}_0^T \mathbf{x}_r \\ &+ \sum_i \lambda_i (\mathbf{x}_r^T \mathbf{P}_i \mathbf{x}_r + \mathbf{q}_i^T \mathbf{x}_r + \varphi_i - r_i) \\ &+ \frac{\rho}{2} \sum_i (\mathbf{x}_r^T \mathbf{P}_i \mathbf{x}_r + \mathbf{q}_i^T \mathbf{x}_r + \varphi_i - r_i)^2, \end{aligned} \quad (21)$$

where $\boldsymbol{\varphi} = [\varphi_1 \dots \varphi_m]^T$ and $\boldsymbol{\lambda} = [\lambda_1 \dots \lambda_m]^T$ are dual variables. In addition, $\rho \geq 0$ is a penalty parameter. We first optimize with respect to $\boldsymbol{\varphi}$, i.e. we solve the following

$$\widehat{\boldsymbol{\varphi}} = \arg \min_{\boldsymbol{\varphi}} \mathcal{L}_\rho(\mathbf{x}_r, \boldsymbol{\varphi}, \boldsymbol{\lambda}), \quad (22)$$

which is solved by taking the gradient of $\mathcal{L}_\rho(\mathbf{x}_r, \boldsymbol{\varphi}, \boldsymbol{\lambda})$ with respect to φ_i , namely

$$\frac{\partial}{\partial \varphi_i} \mathcal{L}_\rho(\mathbf{x}_r, \boldsymbol{\varphi}, \boldsymbol{\lambda}) = \rho (\mathbf{x}_r^T \mathbf{P}_i \mathbf{x}_r + \mathbf{q}_i^T \mathbf{x}_r + \varphi_i - r_i) + \lambda_i, \quad (23)$$

if $\varphi_i \geq 0$, and zero otherwise. Setting the gradient to zero, we get the following update equation

$$\varphi_i^{(n)} = \left[-\frac{\lambda_i}{\rho} - \mathbf{x}_r^T \mathbf{P}_i \mathbf{x}_r - \mathbf{q}_i^T \mathbf{x}_r + r_i \right]^+. \quad (24)$$

Replacing (24) in (21), we get

$$\begin{aligned} \widehat{\mathcal{L}}_\rho(\mathbf{x}_r, \boldsymbol{\lambda}) &= \mathbf{x}_r^T \mathbf{P}_0 \mathbf{x}_r + \mathbf{q}_0^T \mathbf{x}_r - \sum_i \frac{\lambda_i^2}{2\rho} \\ &+ \frac{\rho}{2} \sum_i \left(\left[\frac{\lambda_i}{\rho} + \mathbf{x}_r^T \mathbf{P}_i \mathbf{x}_r + \mathbf{q}_i^T \mathbf{x}_r - r_i \right]^+ \right)^2. \end{aligned} \quad (25)$$

At this point, the optimization with respect to \mathbf{x}_r is achieved by solving

$$\mathbf{x}_r^{(n)} = \arg \min_{\mathbf{x}_r} \widehat{\mathcal{L}}_\rho(\mathbf{x}_r, \boldsymbol{\lambda}^{(n-1)}). \quad (26)$$

The optimization problem in (26) is an unconstrained non-linear optimization problem. As the Hessian is too expensive to compute at every iteration, we resort to a Quasi-Newton type method which can approximate the Hessian matrix via successive iterates based on the gradients of $\widehat{\mathcal{L}}_\rho(\mathbf{x}_r, \boldsymbol{\lambda}^{(n-1)})$ with respect to \mathbf{x}_r . For this, we propose to solve (26) using the Broyden-Fletcher-Goldfarb-Shanno (BFGS) algorithm. Finally, the dual variables are updated as

$$\lambda_i^{(n)} = \lambda_i^{(n-1)} + \rho \left((\mathbf{x}_r^{(n)})^T \mathbf{P}_i \mathbf{x}_r^{(n)} + \mathbf{q}_i^T \mathbf{x}_r^{(n)} + \varphi_i^{(n)} - r_i \right), \quad (27)$$

which can be re-expressed as

$$\lambda_i^{(n)} = \left[\lambda_i^{(n-1)} + \rho \left((\mathbf{x}_r^{(n)})^T \mathbf{P}_i \mathbf{x}_r^{(n)} + \mathbf{q}_i^T \mathbf{x}_r^{(n)} - r_i \right) \right]^+. \quad (28)$$

The summarize steps are given in **Algorithm 1**.

Algorithm 1 BCCD algorithm tailored for DRIP

- 1: INPUT: $\mathbf{x}_{\text{comm}}, \mathbf{x}_0, \eta, \epsilon, \rho$
 - 2: SET: $\mathbf{P}_0 = \mathbf{P}_1 = \mathbf{I}, \mathbf{P}_2 = -\mathbf{I}, \mathbf{P}_3 = \mathbf{I},$
 $\mathbf{q}_0 = -2\phi(\mathbf{x}_{\text{comm}}), \mathbf{q}_1 = \mathbf{q}_2 = \mathbf{0}, \mathbf{q}_3 = -2\phi(\mathbf{x}_0)$
 $r_1 = 1$ and $r_2 = -1, r_3 = \|\mathbf{x}_0\|^2 - \epsilon^2.$
 FOR $p = 1 \dots N_T L$
 $\mathbf{P}_{p+3} = \phi(\mathbf{F}_p), \mathbf{q}_{p+3} = \mathbf{0}, r_{p+3} = \frac{\eta}{N_T L}.$
 - 3: INITIALIZE:
 - 4: $\mathbf{x}^{(0)} = \mathbf{x}_0, \mathbf{x}_r^{(0)} = \phi(\mathbf{x}^{(0)}).$
 - 5: FOR $k = 1 \dots K_{\text{iter}}$ (outer-loop)
 - 6: FOR $q = 1 \dots Q$
 Following (17), update the beamformers as

$$\widehat{\mathbf{u}}_q^{(k)} = \frac{\mathbf{T}_{2,q}^{-1}(\mathbf{I}_L \otimes \boldsymbol{\Pi}(\theta_{q'})) \mathbf{x}^{(k-1)}}{\mathbf{x}^{(k-1)H} (\mathbf{I}_L \otimes \boldsymbol{\Pi}(\theta_{q'})^H \mathbf{T}_{2,q}^{-1}(\mathbf{I}_L \otimes \boldsymbol{\Pi}(\theta_{q'})) \mathbf{x}^{(k-1)}}$$

 Using $\widehat{\mathbf{u}}_q^{(k)}$, and following (31) and (32), compute

$$\mathbf{S}_{1,q}^{(k)} = \sigma_q^2 (\mathbf{I}_L \otimes \boldsymbol{\Pi}(\theta_q))^H \widehat{\mathbf{u}}_q^{(k)} (\widehat{\mathbf{u}}_q^{(k)})^H (\mathbf{I}_L \otimes \boldsymbol{\Pi}(\theta_q))$$

$$\mathbf{S}_{2,q}^{(k)} = \sum_{q' \neq q} \sigma_{q'}^2 (\mathbf{I}_L \otimes \boldsymbol{\Pi}(\theta_{q'}))^H \widehat{\mathbf{u}}_q^{(k)} (\widehat{\mathbf{u}}_q^{(k)})^H (\mathbf{I}_L \otimes \boldsymbol{\Pi}(\theta_{q'}))$$

$$+ \sum_i \bar{\sigma}_i^2 (\mathbf{I}_L \otimes \boldsymbol{\Pi}(\bar{\theta}_i))^H \widehat{\mathbf{u}}_q^{(k)} (\widehat{\mathbf{u}}_q^{(k)})^H (\mathbf{I}_L \otimes \boldsymbol{\Pi}(\bar{\theta}_i))$$

 Fix $\mathbf{q}_{N_T L+3+q} = \mathbf{0}$. Given $\mathbf{S}_{1,q}^{(k)}, \mathbf{S}_{2,q}^{(k)}, \widehat{\mathbf{u}}_q^{(k)}$, compute

$$\mathbf{P}_{N_T L+3+q} = \phi(\bar{g}_q \mathbf{S}_{2,q}^{(k)} - \mathbf{S}_{1,q}^{(k)}),$$

$$r_{N_T L+3+q} = -\bar{g}_q \|\widehat{\mathbf{u}}_q^{(k)}\|^2$$
 - 7: END FOR
 - 8: Initialize $\boldsymbol{\lambda}^{(0)} = \mathbf{0}$
 - 9: FOR $n = 1 \dots N_{\text{iter}}$ (inner-loop)
 Obtain $\mathbf{x}_r^{(n)}$ by solving (26) by the BFGS algorithm.
 Update $\lambda_i^{(n)}$ via (28).
 - 10: END FOR
 - 11: Set $\mathbf{x}^{(k)} = \phi^{-1}(\mathbf{x}_r^{(N_{\text{iter}})})$.
 - 12: return $\mathbf{x}^{(k)}$.
 - 13: END FOR
-

V. CONVERGENCE ANALYSIS

In this section, we perform a convergence analysis of the proposed BCCD algorithm dedicated to generate DRIP-type waveforms. We start by proving convergence of the inner-loop, which is detailed in the following theorem.

Theorem 1: (Inner-loop convergence) If for every $\epsilon_1 > 0$ and $\epsilon_2 > 0$ we can find an iteration N , such that for all iterations $n > N$, we

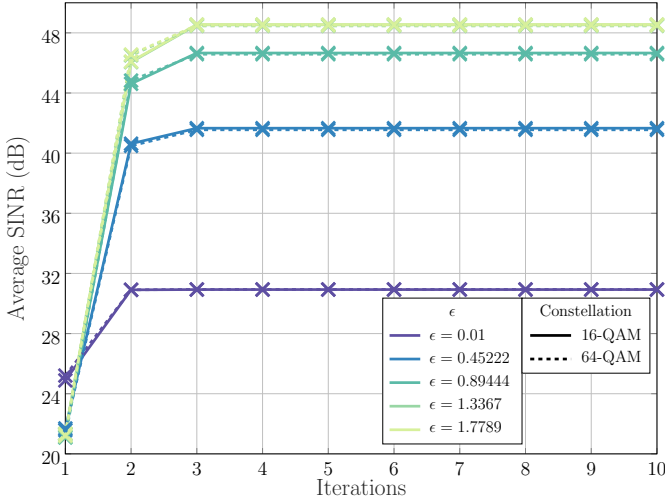


Fig. 2. Average radar SINR of the first target over iterations, when two targets are present at $\theta_1 = 10^\circ$ and $\theta_2 = 30^\circ$. The number of Tx antennas is $N_T = 12$, the signal length $L = 7$, the number of communication users $P = 4$ users, and $\eta = 2.5$ dB. The radar SINR constraint levels are set to $\bar{g}_1 = \bar{g}_2 = 20$ dB.

can bound $\left| (\mathbf{x}_r^{(n+1)})^T \mathbf{P}_i \mathbf{x}_r^{(n+1)} - \bar{\mathbf{x}}_r^T \mathbf{P}_i \bar{\mathbf{x}}_r \right| \leq \epsilon_1$ and $\left| \mathbf{q}_i^T \mathbf{x}_r^{(n+1)} - \mathbf{q}_i^T \bar{\mathbf{x}}_r \right| \leq \epsilon_2, \forall i$, then the algorithm is guaranteed convergence towards $\bar{\mathbf{x}}_r$.

Proof: See Appendix B.

Theorem 1 only proves convergence of the inner-loop of **Algorithm 1**, which is necessary but not a sufficient condition for the convergence of the algorithm. To prove convergence of the algorithm, we must prove convergence of the outer-loop, which is given in the next theorem.

Theorem 2: (Outer-loop convergence) The BCCD iterative method designed in **Algorithm 1**, is guaranteed to converge towards a feasible DRIP solution, i.e. the converged waveform should satisfy the constraints of optimization problem ($\tilde{\mathcal{P}}_{\text{DRIP}}$) given in (13).

Proof: See Appendix C.

VI. SIMULATION RESULTS

In this section, numerical simulation results for characterizing the performance and trade-offs of the proposed DFRC-waveform design are presented. The number of receive antennas is fixed to $N_R = 7$ antennas. The number of radar targets is $Q = 2$ targets and the number of interferers is set to $I = 1$. Furthermore, the communication channel \mathbf{H} is Rayleigh i.i.d distributed. The radar noise variance is set to $\sigma_v^2 = 0.01$. Moreover, The BFGS number of iterations are set to 50. The penalty factor is set to $\rho = 10$. The utilized chirp for sensing is a linear frequency modulation (LFM) chirp.

a) *Convergence behavior of BCCD for DRIP:* In Fig. 2, the radar SINR performance is studied over iteration number of **Algorithm 1**, i.e. the BCCD algorithm for DRIP. In this simulation, the following parameters are used: $N_T = 12$, $L = 7$, $P = 4$, and $\eta = 2.5$ dB. Two targets are set in the scene at $\theta_1 = 10^\circ$ and $\theta_2 = 30^\circ$. Here, the average SINR is shown for the first target. For all iterations, the radar SINR measured at this target is above the 20 dB constraint imposed

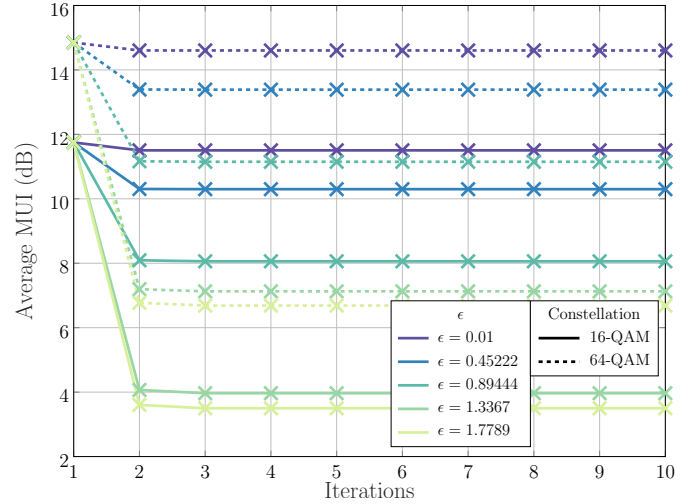


Fig. 3. Average MUI over optimization iterations. The same parameters are set as that of Fig. 2.

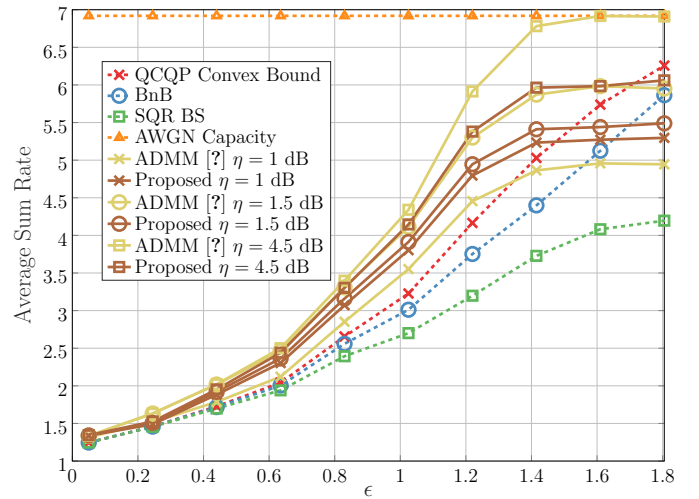


Fig. 4. The performance of the proposed waveform in terms of average sum rate vs. similarity rate. The number of Tx antennas is $N_T = 12$, the signal length $L = 7$, and the number of communication users $P = 4$ users.

by $\bar{g}_1 = \bar{g}_2 = 20$ dB. We can see that the SINR increases steadily before reaching a converging ceiling typically at the third iteration. We can see that in this case, the SINR at this target increases with ϵ . This is because a loose similarity constraint allows for a more optimistic SINR beamforming towards the targets, making the signal power more concentrated to the different target directions, hence exceeding the thresholds specified by \bar{g}_1 and \bar{g}_2 . This can also be seen in Fig. 8. Also, an increase in the QAM size slightly gives a less average SINR at convergence.

In Fig. 3, we study the convergence behaviour of the communication MUI cost with iteration number. In this simulation, the same parameters are set as that of Fig. 2. Also, with a looser ϵ constraint, we can see a decrease in the MUI floor, which implies higher communication rate. With the constellation increasing from 16-QAM to 64-QAM, we observe a rough increase of about 3 dB over all MUI values. This is because more symbols are being transmitted under a

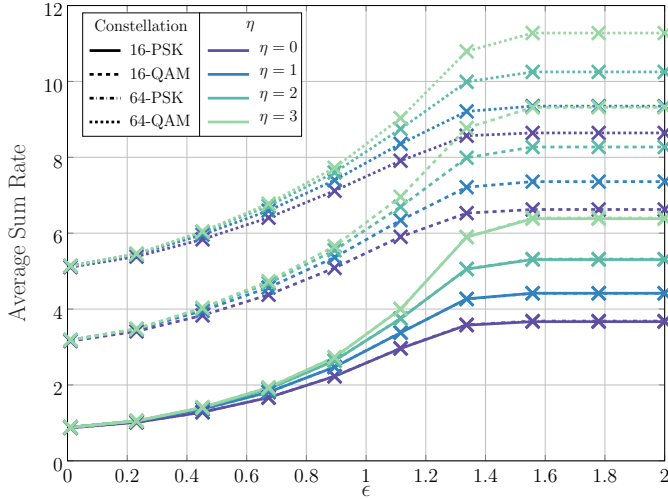


Fig. 5. Average sum rate of the proposed waveform over ϵ . The number of Tx antennas is 12, the signal length $L = 7$, and the number of communication users $P = 4$.

fixed transmit power, which translates into increased MUI. In all cases, we can observe convergence in a few iterations.

b) DRIP rate-similarity tradeoffs: In Fig. 4 and Fig. 5, we study the trade-off between average communication sum rate and similarity constraint with the radar chirp. In this simulation, the following parameters are used: the number of transmit antennas is set to $N_T = 4$, the number of communication users is fixed to $P = 2$, and the utilized modulation scheme is quadrature phase shift keying (QPSK). The waveform length is set to $L = 7$ samples.

In Fig. 4, the proposed waveform is compared with other methods and benchmarks, especially with our previously proposed approach, i.e. SRIP [41]. *A very important note herein is that all other methods do not incorporate beamforming capabilities and only optimize the transmit waveform signal over the temporal domain.* Note that when the radar similarity rate is very stringent ($\epsilon \rightarrow 0$), then all methods exhibit a low average sum rate. For example, at $\epsilon = 0.05$, all methods operate at a similar sum rate of 1.25 bps/Hz. As ϵ increases, i.e. when the radar constraint becomes less demanding, we have interesting observations. When a low PAPR ISAC signal is desired, such as the case of $\eta = 1$ dB, the proposed method, i.e. DRIP, performs better than that in [41]. In particular, it can achieve better communication performance under the same sensing similarity constraint as compared to SRIP [41], the branch and bound (BnB) method in [43], and the successive QCQP refinement binary search (SQR BS) method introduced in [44]. More specifically, when $\epsilon = 1.025$ which can be thought of as midway between radar similarity and communications, DRIP attains an average sum rate of 3.8 bps/Hz, whereas SRIP achieves 3.5 bps/Hz. Moreover, BnB and SQR BS achieve 3 bps/Hz and 2.7 bps/Hz, respectively. This is because, for low PAPR, the dual beam-similarity constraints can better assist for radar tasks leaving more efficient resources for MUI communication performance. For a loose ϵ , DRIP can achieve an average sum rate of up to 6 bps/Hz. However, at higher η values, SRIP outperforms

DRIP and can achieve the AWGN capacity. For example, at $\epsilon = 1.225$, SRIP outperforms the proposed method by roughly 0.6 bps/Hz at $\eta = 4.5$ dB and by roughly 0.5 bps/Hz at $\eta = 1.5$ dB. This is because by including the target SINR constraint in the optimization problem, beamforming towards the target is introduced, which is in favor of radar functionality, hence sacrificing communication performance.

In Fig. 5, the proposed DRIP waveforms for different η and modulation schemes are compared. In this simulation, the following parameters are used: the number of Tx antennas is $N_T = 12$, the signal length $L = 7$, and the number of communication users $P = 4$ users. In general, increasing ϵ promotes a higher average sum rate. This is because imposing a less stringent similarity constraint with the radar chirp allows for further minimization of the MUI communication cost. Also, with the increase in η , the sum rate increases as well. This is especially obvious at higher ϵ . For example, for $\epsilon \geq 1.5578$, the gain in sum rate for all constellations through increasing η from 0 dB to 3 dB is roughly 2.4 bps/Hz. A gain from changing the constellation from PSK to QAM can also be seen. For example, the change from 16 PSK to 16 QAM brings gain of about 2.3 bps/Hz. This is because conventional QAM generally has better communication performance than PSK [45], [46]. Generally speaking, QAM is preferred in communication than PSK due to its wider decision regions, decreasing the error rate. On the other hand, PSK is more preferred for sensing due to its higher similarity than Gaussian symbols.

c) ϵ -dependent DRIP constellations: In Fig. 6, the constellation of DRIP waveforms are characterized over multiple ϵ values. In this simulation, the following parameters are used: the number of Tx antennas is $N_T = 12$, the signal length $L = 7$, the number of communication users is $P = 5$, and $\eta = 6$ dB. By increasing ϵ , minimizing the MUI is prioritized over similarity with radar waveforms, making the constellations more similar to the respective communication constellations. At high ϵ values most notable beyond 1.5578, we can see the constellation resembles a clear QPSK (in Fig. 6a) or 16-PSK shape (in Fig. 6b). This is because more priority is imposed over communications. Now, by decreasing ϵ , similarity with radar waveforms becomes more stringent and becomes the dominating factor over MUI, making the constellations blurry while concentrated around the origin. This is because a low ϵ enforces the transmitted symbols to be more similar to the chirp close to having the ideal radar constellation.

d) Dual sensing trade-offs: In Fig. 7, we study the trade-off within sensing between prioritizing target SINR and similarity with the chirp. The same parameters are set as that of Fig. 2. We notice that an increase in ϵ contributes to an increase in average radar SINR across all the involved targets of interest. In particular, an increase in radar SINR necessitates a sacrifice in similarity rate for a fixed \bar{g}_q . This is because, for fixed power, relaxing the temporal domain constraint over the radar similarity chirp leaves more opportunity for an increase in target SINR. In addition, the PSK constellations can give an even more SINR performance across targets than the QAM constellations. For example, at $\epsilon = 1.3367$, 16-QAM gives an

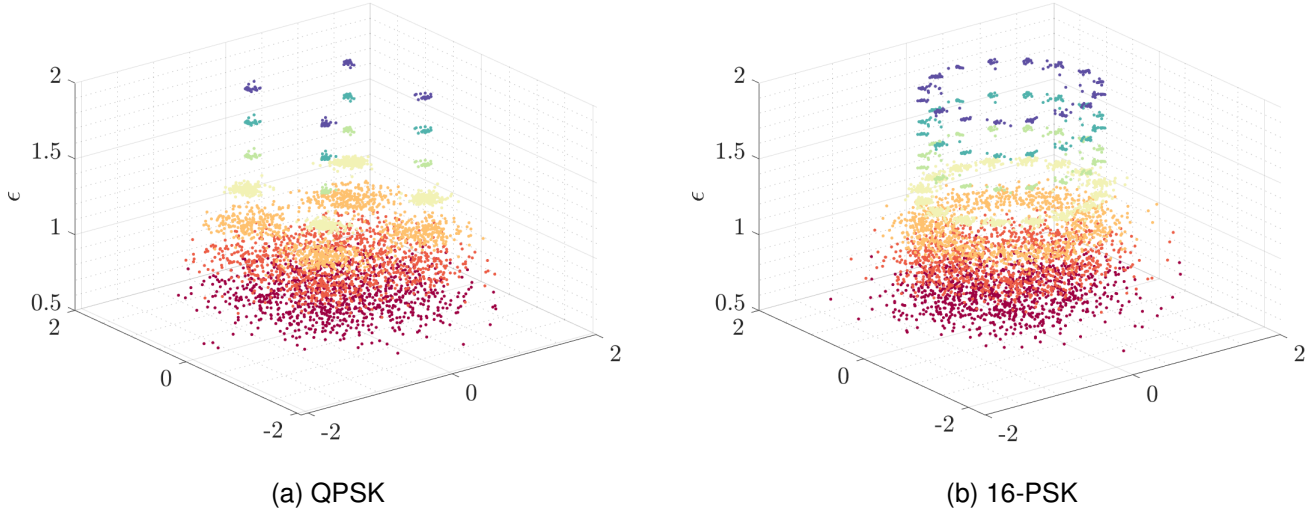


Fig. 6. DRIP constellations over varying ϵ values. The number of Tx antennas is 12, the signal length $L = 7$, the number of communication users $P = 5$, and $\eta = 6$ dB. The x and y axis represent the in-phase and quadrature components of the constellations.

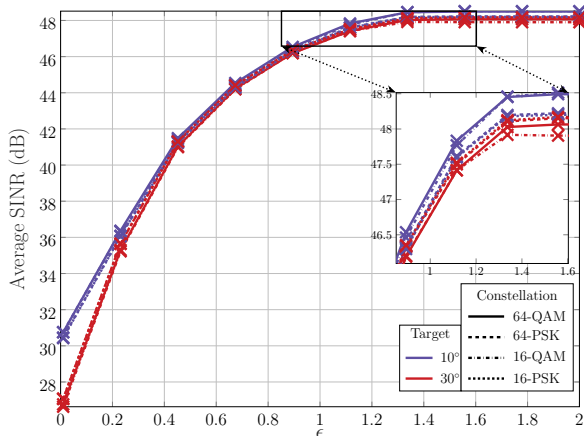


Fig. 7. Trade-off within sensing between target SINR and ϵ . The same parameters are set as that of Fig. 2.

SINR disparity between targets of about 0.6 dB, while 16-PSK gives about 0.1 dB.

e) DRIP beampatterns: In Fig. 8, we plot the beam-pattern of the proposed DRIP waveforms, which is obtained by steering the SINR over angles from -90° to 90° . In this simulation, the same parameters are set as that of Fig. 2, except for $\eta = 2.5$ dB and the utilized constellation was a 64-QAM. When we lower the ϵ , thus making the waveform more similar to a radar chirp, we can achieve better sidelobe performances but very ambiguous peaks, meaning that the beamforming is not ideal. As ϵ increases, the DRIP beampattern tends to point towards the targets of interest, which is translated to sharp peaks towards the targets of interest. By comparing Fig. 8a with Fig. 8b, we can also observe that when the targets are further away, *clearer peaks can be achieved even at lower ϵ values, which translates into improved DRIP spatial*

resolution. For example, at $\epsilon = 0.45222$, Fig. 8b shows two clear peaks of about 48 dB and 43 dB at the desired target locations while its counterpart, Fig. 8a. only shows an ambiguous plateau of around 37 dB between 0° and 40° .

f) DRIP PAPR CCDF statistics: In Fig. 9, we analyze the complementary cumulative distribution function (CCDF) of the PAPR values under different η . The parameters N_T , L and P are the same as in Fig. 8. Fig. 9a shows how the CCDF distribution of the PAPR distribution varies with different η , at a fixed ϵ , which is fixed to $\epsilon = 0.01$. As the η constraint loosens, the distribution of PAPR spreads more to higher values as expected. In fact, the CCDF of PAPRs converges to a certain distribution when η grows large. This is because the actual PAPRs of the DRIP waveforms live beyond these large η values, hence after a certain η , it is "as if" the PAPR constraint becomes inactive. For instance, at $\eta \geq 3$ dB, we observe similar distributions across all η values. In addition, the PAPR distribution tends to higher values when the constellation size is increased. Fig. 9b shows how the PAPR distribution varies with ϵ , for a fixed constellation. In this simulation, we fix the modulation to 16-QAM. As expected, a looser ϵ promotes DRIP waveforms of higher PAPR levels. Also, we can see that at high ϵ , the PAPR is strongly restricted by η . This is because DRIP waveforms become primarily constrained by the PAPR constraint instead of the similarity constraint.

g) DRIP MUI variability with similarity: In Fig. 10, we study the distribution of the MUI, which is directly related to the sum rate for a fixed constellation, with respect to ϵ . In this simulation, the following parameters are used: the number of Tx antennas is 12, the signal length $L = 7$, the number of communication users $P = 4$, and the modulation used is 16-QAM. Lower median MUI values with higher variations of MUI are observed at higher values of ϵ . For example, when $\epsilon = 1.33$, the median MUI of DRIP waveforms at $\eta = 6$ dB is 0.69 dB with the lower and upper whiskers corresponding to -0.38 dB and 2.07 dB, respectively, which is an MUI gap of

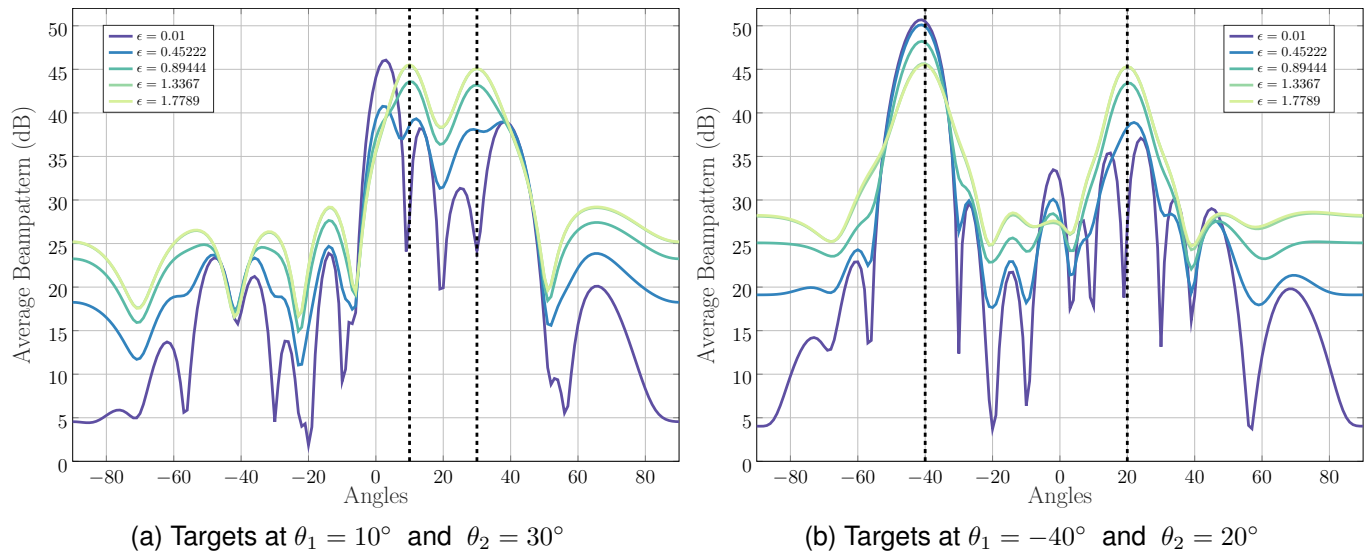


Fig. 8. Resulting beampatterns for different 2-target configurations. The number of transmit antennas is $N_T = 12$, the signal length $L = 7$, the number of communication users $P = 4$, $\eta = 2.5$ dB and the utilized constellation was a 64-QAM. Dotted vertical lines correspond to the true target locations.

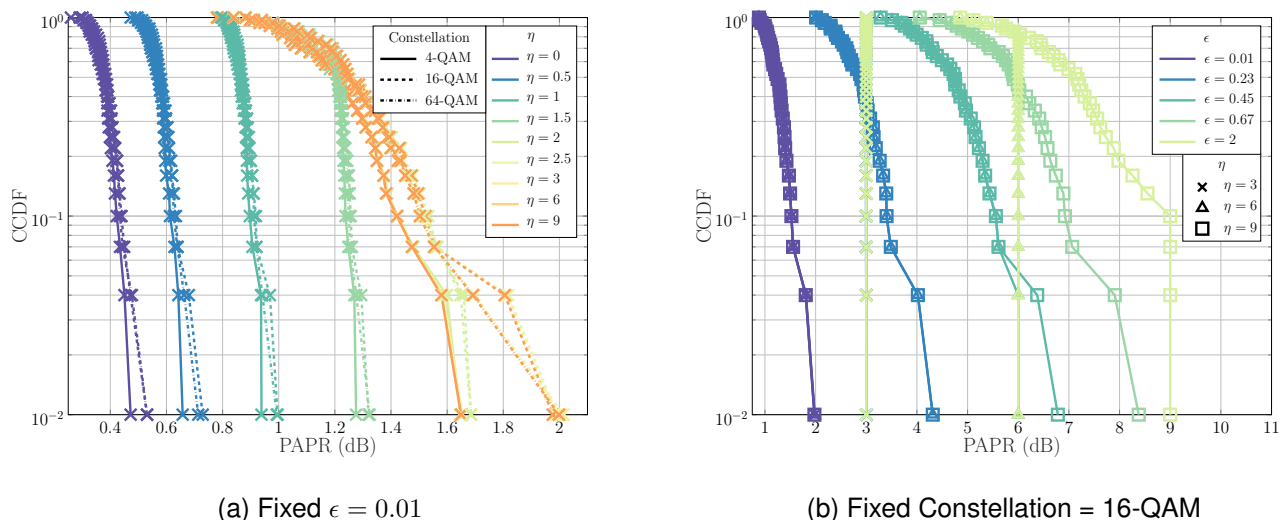


Fig. 9. CCDF of PAPR for two different sets of testing parameters. The parameters N_T , L and P are the same as in Fig. 8.

2.45 dB. When $\epsilon \geq 1.55$, the median MUI drastically drops to -3.61 dB with an MUI gap becomes 3.69 dB. Generally speaking, as ϵ increases, the median MUI values of DRIP waveforms decreases with an increase in MUI whisker gaps, i.e. more variability in MUI.

In Fig. 11, we illustrate the average MUI behavior, which has an impact on the communication rate, with increasing η and different ϵ values. In this simulation, the following parameters are used: the number of Tx antennas is $N_T = 12$, the signal length $L = 7$, the number of communication users $P = 4$ users, and the modulation used is 16-QAM. The higher the η , the less the MUI cost. This is because it allows for larger PAPR, making it closer to an ideal communication waveform. We can see the trade off between η and ϵ along with their impact on MUI. For low ϵ values (i.e. $\epsilon \leq 1.11$), the prioritizing of similarity manifests as the “floor” at high eta,

when the PAPR constraint is loose. For higher ϵ , the curves coincide. In particular, for $\epsilon \geq 1.55$, the behavior of MUI vs. η is the same, meaning that increasing ϵ beyond 1.55 does not help much with obtaining a better communication rate. However, we can see that the MUI floor (appearing only for lower ϵ values) disappears, which is more favorable for communications. Hence, combined with discussions Fig. 12, if we want to prioritize communications, we can mainly increase ϵ in the S-constrained region and η in the C-constrained region. If we want to prioritize sensing similarity, which gives better space resolution of targets, we can decrease ϵ in the S-constrained region but the performance does not respond much to the tuning of any parameters in the C-constrained region.

h) Sensing and Communication Regions: In Fig. 12, we intend to illustrate the sensing (denoted as S) and communication (denoted as C) regions. Specifically, the curve shown

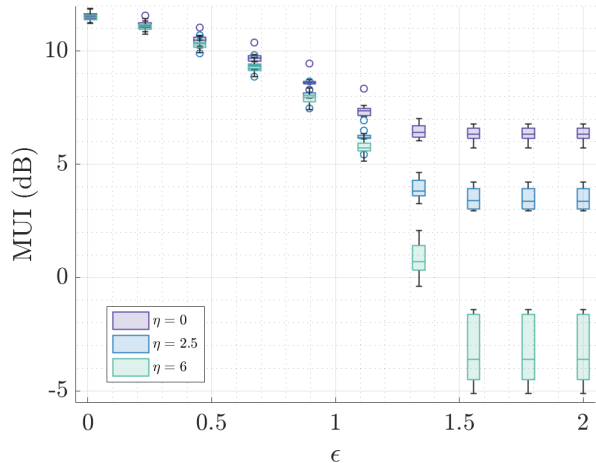


Fig. 10. MUI distribution with respect to ϵ . The number of Tx antennas is 12, the signal length $L = 7$, the number of communication users $P = 4$, and the modulation used is 16-QAM.

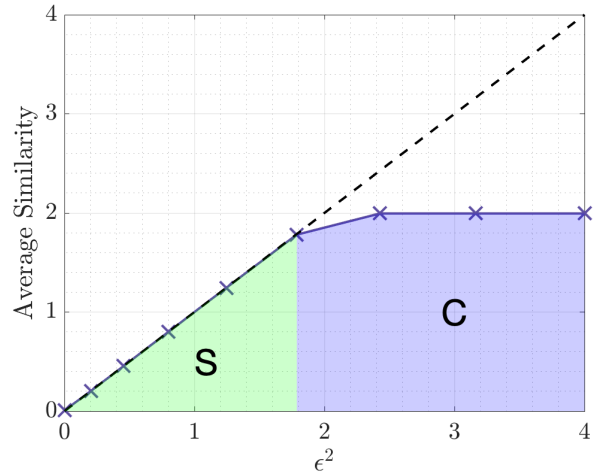


Fig. 12. Average empirical similarity with the radar chirp with respect to ϵ . The curve shown is get from all variations of η , \bar{g}_q , and constellations.

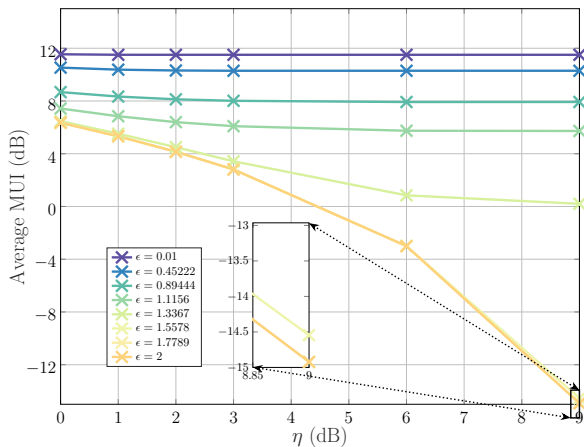


Fig. 11. Average MUI with respect to η . The number of Tx antennas is 12, the signal length $L = 7$, the number of communication users $P = 4$, and the modulation used is 16-QAM.

is obtained by varying a wide range of η values spanning 0 dB to 9 dB, a wide range of \bar{g}_q from 10 dB and 20 dB, and different constellations of QPSK, 16-QAM, 64-QAM, 16-PSK, and 64-PSK. It can be seen that the average empirical similarity is always constrained by ϵ . For $\epsilon^2 \leq 1.78$ values, the similarity measure changes with ϵ and attains the constraint with equality as the average similarity is on the straight line. This is because the DRIP waveforms favor the similarity constraint, $\mathcal{B}_\epsilon(\mathbf{x}_0)$, hence the reason we quantify this region as the S-region. When, $\epsilon^2 \geq 1.78$, the DRIP waveforms favor the communication constellations and no longer adhere to the sensing chirp waveforms, therefore the waveforms enter the C-region.

VII. CONCLUSIONS

In this paper, we introduced DRIP, which is a family of space-time ISAC waveforms capable of PAPR adjustment. The

proposed space-time ISAC waveforms, i.e. DRIP, abide by given PAPR levels, while remaining similar to a given radar chirp, maintaining good beampattern properties towards desired directions, and rejecting interfering ones for multi-target sensing applications. As for communications, the proposed DRIP waveforms intend to minimize MUI for any given constellation. As the optimization framework intended to generate such space-time ISAC waveforms is challenging to solve, we propose a BCCD method that iterates between the different variables of the problem, which is guaranteed to converge to a waveform. Finally, simulation results demonstrate the superior performance, versatility, as well as ISAC trade-offs of the proposed family of space-time ISAC waveforms.

APPENDIX A PROOF OF PROPERTY 1

In this part of the appendix, we prove that the problem in (18) is QCQP. Before we proceed, and for convenience, we define complex-to-real operators of vectors and matrices as

$$\phi(\mathbf{x}) = [\text{Re}^T(\mathbf{x}) \quad \text{Im}^T(\mathbf{x})]^T, \quad (29)$$

$$\phi(\mathbf{A}) = \begin{bmatrix} \text{Re}(\mathbf{A}) & -\text{Im}(\mathbf{A}) \\ \text{Im}(\mathbf{A}) & \text{Re}(\mathbf{A}) \end{bmatrix}. \quad (30)$$

Next, we translate each term appearing in (18) to match the form of $(\mathcal{S}_{\text{QCQP}})$ given in (19). The complex-valued variable in (18) corresponds to \mathbf{x}_r as $\mathbf{x}_r = \phi(\mathbf{x})$. The cost in (18) is quadratic in \mathbf{x}_r , and hence we can pick $\mathbf{P}_0 = \mathbf{I}$ and $\mathbf{q}_0 = -2\phi(\mathbf{x}_{\text{comm}})$ to match the non-constant terms of the cost in (19). The norm-equality constraint in (18), i.e. $\|\mathbf{x}\|^2 = 1$, can be replaced by two inequality constraints, i.e. $\|\mathbf{x}_r\|^2 \leq 1$ and $\|\mathbf{x}_r\|^2 \geq 1$. Hence, choosing $\mathbf{P}_1 = \mathbf{I}$, $\mathbf{P}_2 = -\mathbf{I}$, $\mathbf{q}_1 = \mathbf{q}_2 = \mathbf{0}$, and $r_1 = 1$ and $r_2 = -1$ account for constraint $\|\mathbf{x}\|^2 = 1$. The sphere constraint in (18) can be represented by picking $\mathbf{P}_3 = \mathbf{I}$, $\mathbf{q}_3 = -2\phi(\mathbf{x}_0)$, and $r_3 = \|\mathbf{x}_0\|^2 - \epsilon^2$. The quadratic-inequality constraint in (18), i.e. $\mathbf{x}^H \mathbf{F}_p \mathbf{x} \leq \frac{\eta}{N_T L}$, can be realized by picking $\mathbf{P}_{p+3} = \phi(\mathbf{F}_p)$, $\mathbf{q}_{p+3} = \mathbf{0}$ and $r_{p+3} = \frac{\eta}{N_T L}$, for all $p = 1 \dots N_T L$. Last but not least, the

radar SINR constraints in (18) can also be arranged via QCQP constraints. In realizing so, we first interchange the role of \widehat{g}_q and \mathbf{x} . For that, we have $\widehat{g}_q = \frac{\mathbf{x}^H \mathbf{S}_{1,q} \mathbf{x}}{\mathbf{x}^H \mathbf{S}_{2,q} \mathbf{x} + \sigma_q^2 \|\widehat{\mathbf{u}}_q\|^2}$, $\forall q = 1 \dots Q$, where

$$\mathbf{S}_{1,q} = \sigma_q^2 (\mathbf{I}_L \otimes \mathbf{\Pi}(\theta_q))^H \widehat{\mathbf{u}}_q \widehat{\mathbf{u}}_q^H (\mathbf{I}_L \otimes \mathbf{\Pi}(\theta_q)) \quad (31)$$

$$\begin{aligned} \mathbf{S}_{2,q} = & \sum_{q' \neq q} \sigma_{q'}^2 (\mathbf{I}_L \otimes \mathbf{\Pi}(\theta_{q'}))^H \widehat{\mathbf{u}}_{q'} \widehat{\mathbf{u}}_{q'}^H (\mathbf{I}_L \otimes \mathbf{\Pi}(\theta_{q'})) \\ & + \sum_i \bar{\sigma}_i^2 (\mathbf{I}_L \otimes \mathbf{\Pi}(\bar{\theta}_i))^H \widehat{\mathbf{u}}_i \widehat{\mathbf{u}}_i^H (\mathbf{I}_L \otimes \mathbf{\Pi}(\bar{\theta}_i)) \end{aligned} \quad (32)$$

Therefore, choosing $\mathbf{P}_{N_T L + 3 + q} = \phi(\bar{g}_q \mathbf{S}_{2,q} - \mathbf{S}_{1,q})$, $\mathbf{q}_{N_T L + 3 + q} = \mathbf{0}$, and $r_{N_T L + 3 + q} = -\bar{g}_q \|\widehat{\mathbf{u}}_q\|^2$ for all $q = 1 \dots Q$ finalizes the proof.

APPENDIX B PROOF OF THEOREM 1

We first take the gradient of (25) with respect to \mathbf{x}_r as

$$\begin{aligned} \nabla_{\mathbf{x}_r} \widehat{\mathcal{L}}_\rho(\mathbf{x}_r, \boldsymbol{\lambda}) = & 2\mathbf{P}_0 \mathbf{x}_r + \mathbf{q}_0 \\ & + \rho \sum_i \left[\frac{\lambda_i}{\rho} + \mathbf{x}_r^T \mathbf{P}_i \mathbf{x}_r + \mathbf{q}_i^T \mathbf{x}_r - r_i \right]^+ \mathbf{g}_i. \end{aligned}$$

where $\mathbf{g}_i = 2\mathbf{P}_i \mathbf{x}_r + \mathbf{q}_i$ if $\frac{\lambda_i}{\rho} + \mathbf{x}_r^T \mathbf{P}_i \mathbf{x}_r + \mathbf{q}_i^T \mathbf{x}_r - r_i \geq 0$, else $\mathbf{g}_i = \mathbf{0}$, which implies that the above gradient can be expressed as

$$\begin{aligned} \nabla_{\mathbf{x}_r} \widehat{\mathcal{L}}_\rho(\mathbf{x}_r, \boldsymbol{\lambda}) = & 2\mathbf{P}_0 \mathbf{x}_r + \mathbf{q}_0 \\ & + \rho \sum_i \left[\frac{\lambda_i}{\rho} + \mathbf{x}_r^T \mathbf{P}_i \mathbf{x}_r + \mathbf{q}_i^T \mathbf{x}_r - r_i \right]^+ (2\mathbf{P}_i \mathbf{x}_r + \mathbf{q}_i). \end{aligned} \quad (33)$$

But notice that when the gradient in (33) is evaluated at $(\mathbf{x}_r^{(n)}, \boldsymbol{\lambda}^{(n-1)})$, and with the aid of (28), it follows that

$$\nabla_{\mathbf{x}_r} \widehat{\mathcal{L}}_\rho^{(n)} = 2\mathbf{P}_0 \mathbf{x}_r^{(n)} + \mathbf{q}_0 + \sum_i \lambda_i^{(n)} (2\mathbf{P}_i \mathbf{x}_r^{(n)} + \mathbf{q}_i), \quad (34)$$

where $\nabla_{\mathbf{x}_r} \widehat{\mathcal{L}}_\rho^{(n)} \triangleq \nabla_{\mathbf{x}_r} \widehat{\mathcal{L}}_\rho(\mathbf{x}_r^{(n)}, \boldsymbol{\lambda}^{(n-1)})$; which means that $\mathbf{x}_r^{(n+1)}$ minimizes $\mathbf{x}_r^T \mathbf{P}_0 \mathbf{x}_r + \mathbf{q}_0^T \mathbf{x}_r + \sum_i \lambda_i^{(n)} (\mathbf{x}_r^T \mathbf{P}_i \mathbf{x}_r + \mathbf{q}_i^T \mathbf{x}_r)$. Denoting

$$\Delta h^{(n)} = (\mathbf{x}_r^{(n+1)})^T \mathbf{P}_0 \mathbf{x}_r^{(n+1)} + \mathbf{q}_0^T \mathbf{x}_r^{(n+1)} - \bar{\mathbf{x}}_r^T \mathbf{P}_0 \bar{\mathbf{x}}_r + \mathbf{q}_0^T \bar{\mathbf{x}}_r, \quad (35)$$

we have that

$$\begin{aligned} \Delta h^{(n)} \leq & \sum_i \lambda_i^{(n)} \left(\bar{\mathbf{x}}_r^T \mathbf{P}_i \bar{\mathbf{x}}_r - (\mathbf{x}_r^{(n+1)})^T \mathbf{P}_i \mathbf{x}_r^{(n+1)} \right) \\ & + \sum_i \lambda_i^{(n)} \left(\mathbf{q}_i^T \bar{\mathbf{x}}_r - \mathbf{q}_i^T \mathbf{x}_r^{(n+1)} \right). \end{aligned} \quad (36)$$

Therefore, as $\lim_{n \rightarrow \infty} (\mathbf{x}_r^{(n+1)})^T \mathbf{P}_i \mathbf{x}_r^{(n+1)} = \bar{\mathbf{x}}_r^T \mathbf{P}_i \bar{\mathbf{x}}_r$ (namely $\left| (\mathbf{x}_r^{(n+1)})^T \mathbf{P}_i \mathbf{x}_r^{(n+1)} - \bar{\mathbf{x}}_r^T \mathbf{P}_i \bar{\mathbf{x}}_r \right| \leq \epsilon_1$ for every $\epsilon_1 > 0$ and a given iteration N for all $n \geq N$) and $\lim_{n \rightarrow \infty} \mathbf{q}_i^T \mathbf{x}_r^{(n+1)} = \mathbf{q}_i^T \bar{\mathbf{x}}_r$ (namely $\left| \mathbf{q}_i^T \mathbf{x}_r^{(n+1)} - \mathbf{q}_i^T \bar{\mathbf{x}}_r \right| \leq \epsilon_2$ for every $\epsilon_2 > 0$ and a given iteration N for all $n \geq N$), we get $\lim_{n \rightarrow \infty} \Delta h^{(n)} = 0$, i.e.

$\lim_{n \rightarrow \infty} \Delta h^{(n)} = 0$ and the algorithm terminates, which finalizes the proof.

APPENDIX C PROOF OF THEOREM 2

At iteration number k , the space-time ISAC waveform and beamforming vectors are assumed to satisfy the DRIP constraints, i.e. the constraints of optimization problem $(\widetilde{\mathcal{P}}_{\text{DRIP}})$ in (13), namely

$$\begin{cases} \|\mathbf{x}^{(k)}\|^2 = 1, \\ (\mathbf{x}^{(k)})^H \mathbf{F}_p \mathbf{x}^{(k)} \leq \frac{\eta}{N_T L}, \quad \forall p \\ \mathbf{x}^{(k)} \in \mathcal{B}_\epsilon(\mathbf{x}_0), \quad g_q(\mathbf{x}^{(k)}, \widehat{\mathbf{u}}_q^{(k)}) \geq \bar{g}_q, \quad \forall q. \end{cases} \quad (37)$$

In the following iteration, $\mathbf{x}^{(k+1)}$ is obtained by solving

$$\begin{cases} \min_{\mathbf{x}} \quad \|\mathbf{x} - \mathbf{x}_{\text{comm}}\|^2 \\ \text{s.t.} \quad \|\mathbf{x}\|^2 = 1, \\ \mathbf{x}^H \mathbf{F}_p \mathbf{x} \leq \frac{\eta}{N_T L}, \quad \forall p \\ \mathbf{x} \in \mathcal{B}_\epsilon(\mathbf{x}_0), \quad g_q(\mathbf{x}, \widehat{\mathbf{u}}_q^{(k+1)}) \geq \bar{g}_q, \quad \forall q, \end{cases} \quad (38)$$

where $\widehat{\mathbf{u}}_q^{(k+1)}$ solves (16), given $\mathbf{x}^{(k)}$. It follows that

$$g_q(\mathbf{x}^{(k)}, \widehat{\mathbf{u}}_q^{(k+1)}) \geq g_q(\mathbf{x}^{(k)}, \widehat{\mathbf{u}}_q^{(k)}) \geq \bar{g}_q, \quad \forall q. \quad (39)$$

In turn, since $(\mathbf{x}^{(k+1)}, \{\widehat{\mathbf{u}}_q^{(k+1)}\}_{q=1}^Q)$ solves (38), then it should satisfy its constraints and hence is a feasible solution. In addition,

$$\|\mathbf{x}^{(k+1)} - \mathbf{x}_{\text{comm}}\|^2 \leq \|\mathbf{x}^{(k)} - \mathbf{x}_{\text{comm}}\|^2. \quad (40)$$

By induction, the algorithm converges and the proof is done.

REFERENCES

- [1] M. Chafii, L. Bariah, S. Muhaidat, and M. Debbah, "Twelve Scientific Challenges for 6G: Rethinking the Foundations of Communications Theory," *IEEE Communications Surveys & Tutorials*, vol. 25, no. 2, pp. 868–904, 2023.
- [2] S. Ehsanfar, A. Bazzi, K. Möbner, and M. Chafii, "Hypothesis Testing on FMCW and OFDM for Joint Communication and Radar in IEEE 802.11bd," in *2023 IEEE International Conference on Communications Workshops (ICC Workshops)*, 2023, pp. 464–469.
- [3] H. El Hammouti, M. Benjillali, B. Shihada, and M.-S. Alouini, "Learn-As-You-Fly: A Distributed Algorithm for Joint 3D Placement and User Association in Multi-UAVs Networks," *IEEE Transactions on Wireless Communications*, vol. 18, no. 12, pp. 5831–5844, 2019.
- [4] H. Elhammouti, E. Sabir, M. Benjillali, L. Echabbi, and H. Tembine, "Self-Organized Connected Objects: Rethinking QoS Provisioning for IoT Services," *IEEE Communications Magazine*, vol. 55, no. 9, pp. 41–47, 2017.
- [5] L. Chen, I. Ahriz, and D. Le Ruyet, "AoA-Aware Probabilistic Indoor Location Fingerprinting Using Channel State Information," *IEEE Internet of Things Journal*, vol. 7, no. 11, pp. 10 868–10 883, 2020.
- [6] Y. Bouazizi, F. Benkelifa, H. ElSawy, and J. A. McCann, "On the Scalability of Duty-Cycled LoRa Networks With Imperfect SF Orthogonality," *IEEE Wireless Communications Letters*, vol. 11, no. 11, pp. 2310–2314, 2022.
- [7] C. Chaccour, W. Saad, M. Debbah, and H. V. Poor, "Joint Sensing, Communication, and AI: A Trifecta for Resilient THz User Experiences," *IEEE Transactions on Wireless Communications*, pp. 1–1, 2024.
- [8] A. Bazzi and M. Chafii, "Secure Full Duplex Integrated Sensing and Communications," *IEEE Transactions on Information Forensics and Security*, vol. 19, pp. 2082–2097, 2024.
- [9] V. Kumar, M. Chafii, A. L. Swindlehurst, L.-N. Tran, and M. F. Flanagan, "SCA-Based Beamforming Optimization for IRS-Enabled Secure Integrated Sensing and Communication," in *GLOBECOM 2023 - 2023 IEEE Global Communications Conference*, 2023, pp. 5992–5997.
- [10] T. S. Rappaport, Y. Xing, O. Kanhere, S. Ju, A. Madanayake, S. Mandal, A. Alkhateeb, and G. C. Trichopoulos, "Wireless Communications and Applications Above 100 GHz: Opportunities and Challenges for 6G and Beyond," *IEEE Access*, vol. 7, pp. 78 729–78 757, 2019.

- [11] R. Alghamdi, H. Dahrouj, T. Al-Naffouri, and M.-S. Alouini, "Toward Immersive Underwater Cloud-Enabled Networks: Prospects and Challenges," *IEEE BITS the Information Theory Magazine*, pp. 1–12, 2023.
- [12] Y. Cui, H. Ding, L. Zhao, and J. An, "Integrated Sensing and Communication: A Network Level Perspective," *IEEE Wireless Communications*, vol. 31, no. 1, pp. 103–109, 2024.
- [13] C. Liaskos, K. Katsalis, J. Triay, and S. Schmid, "Resource Management for Programmable Metasurfaces: Concept, Prospects and Challenges," *IEEE Communications Magazine*, vol. 61, no. 11, pp. 208–214, 2023.
- [14] F. Liu, L. Zheng, Y. Cui, C. Masouros, A. P. Petropulu, H. Griffiths, and Y. C. Eldar, "Seventy Years of Radar and Communications: The road from separation to integration," *IEEE Signal Processing Magazine*, vol. 40, no. 5, pp. 106–121, 2023.
- [15] Y. Cui, F. Liu, X. Jing, and J. Mu, "Integrating Sensing and Communications for Ubiquitous IoT: Applications, Trends, and Challenges," *IEEE Network*, vol. 35, no. 5, pp. 158–167, 2021.
- [16] F. Liu, Y. Cui, C. Masouros, J. Xu, T. X. Han, Y. C. Eldar, and S. Buzzi, "Integrated Sensing and Communications: Toward Dual-Functional Wireless Networks for 6G and Beyond," *IEEE Journal on Selected Areas in Communications*, vol. 40, no. 6, pp. 1728–1767, 2022.
- [17] Z. Wei, F. Liu, C. Masouros, N. Su, and A. P. Petropulu, "Toward Multi-Functional 6G Wireless Networks: Integrating Sensing, Communication, and Security," *IEEE Communications Magazine*, vol. 60, no. 4, pp. 65–71, 2022.
- [18] J. An, H. Li, D. W. K. Ng, and C. Yuen, "Fundamental Detection Probability vs. Achievable Rate Tradeoff in Integrated Sensing and Communication Systems," *IEEE Transactions on Wireless Communications*, vol. 22, no. 12, pp. 9835–9853, 2023.
- [19] C. Ouyang, Y. Liu, H. Yang, and N. Al-Dhahir, "Integrated Sensing and Communications: A Mutual Information-Based Framework," *IEEE Communications Magazine*, vol. 61, no. 5, pp. 26–32, 2023.
- [20] 3rd Generation Partnership Project (3GPP), "Editorial clean-up of TR 22.837 section 7," SA1#105, SA#103 SA WG1 19.3.0 FS_Sensing, Deutsche Telekom AG, Technical Report 22.837, March 2024, details S1-240119 agreed, Details SP-240202 approved.
- [21] C. Wen, Y. Huang, and T. N. Davidson, "Efficient Transceiver Design for MIMO Dual-Function Radar-Communication Systems," *IEEE Transactions on Signal Processing*, vol. 71, pp. 1786–1801, 2023.
- [22] L. Meilhac and A. Bazzi, "Digital pre-distortion method for OFDM-based communication systems," Apr. 12 2022, US Patent 11,303,310.
- [23] M. Chafii, J. Palicot, R. Gribonval, and F. Bader, "A Necessary Condition for Waveforms With Better PAPR Than OFDM," *IEEE Transactions on Communications*, vol. 64, no. 8, pp. 3395–3405, 2016.
- [24] X. Wang, N. Jin, and J. Wei, "A Model-Driven DL Algorithm for PAPR Reduction in OFDM System," *IEEE Communications Letters*, vol. 25, no. 7, pp. 2270–2274, 2021.
- [25] Y. Zhou, Y. Yang, Z. Zhou, K. Anand, S. Hu, and Y. L. Guan, "New Complementary Sets With Low PAPR Property Under Spectral Null Constraints," *IEEE Transactions on Information Theory*, vol. 66, no. 11, pp. 7022–7032, 2020.
- [26] X. Zhao and Y.-J. A. Zhang, "Joint Beamforming and Scheduling for Integrated Sensing and Communication Systems in URLLC: A POMDP Approach," *IEEE Transactions on Communications*, pp. 1–1, 2024.
- [27] X. Wang, W. Zhai, X. Wang, M. G. Amin, and K. Cai, "Wideband Near-Field Integrated Sensing and Communication With Sparse Transceiver Design," *IEEE Journal of Selected Topics in Signal Processing*, pp. 1–16, 2024.
- [28] Z. Li, F. Hu, Q. Li, Z. Ling, Z. Chang, and T. Hämäläinen, "AoI-Aware Waveform Design for Cooperative Joint Radar-Communications Systems with Online Prediction of Radar Target Property," *IEEE Transactions on Communications*, pp. 1–1, 2024.
- [29] Q. Lu, Z. Du, and Z. Zhang, "OFDM Waveform Design with Subcarrier Interval Constraint for Narrowband Interference Suppression in ISAC Systems," *IEEE Communications Letters*, pp. 1–1, 2024.
- [30] D. Luo, F. Gao, Z. Ye, F. Yu, and H. Wu, "Beamspace Waveform Design and Beam Selection for Lens Antenna Array-Assisted ISAC Systems," *IEEE Wireless Communications Letters*, pp. 1–1, 2024.
- [31] X. Liu, Y. Yuan, T. Zhang, G. Cui, and W. P. Tay, "Integrated Transmit Waveform and RIS Phase Shift Design for LPI Detection and Communication," *IEEE Transactions on Wireless Communications*, pp. 1–1, 2023.
- [32] B. Guo, J. Liang, B. Tang, L. Li, and H. C. So, "Bistatic MIMO DFRC System Waveform Design via Symbol Distance/Direction Discrimination," *IEEE Transactions on Signal Processing*, vol. 71, pp. 3996–4010, 2023.
- [33] Z. Wei, J. Piao, X. Yuan, H. Wu, J. A. Zhang, Z. Feng, L. Wang, and P. Zhang, "Waveform Design for MIMO-OFDM Integrated Sensing and Communication System: An Information Theoretical Approach," *IEEE Transactions on Communications*, vol. 72, no. 1, pp. 496–509, 2024.
- [34] X. Liu, Y. Yang, J. Gong, N. Xia, J. Guo, and M. Peng, "Amplitude Barycenter Calibration of Delay-Doppler Spectrum for OTFS Signal—An Endeavor to Integrated Sensing and Communication Waveform Design," *IEEE Transactions on Wireless Communications*, vol. 23, no. 4, pp. 2622–2637, 2024.
- [35] Y. Yang, Y. Pan, X. Liu, and M. Peng, "Barycenter Calibration with High Order Spectra of Windowed Delay-Doppler Signals for OTFS based ISAC Systems," *IEEE Transactions on Signal Processing*, pp. 1–16, 2024.
- [36] K. Zhang, W. Yuan, P. Fan, and X. Wang, "Dual-Functional Waveform Design with Local Sidelobe Suppression via OTFS Signaling," *IEEE Transactions on Vehicular Technology*, pp. 1–6, 2024.
- [37] J. Zou, S. Sun, C. Masouros, Y. Cui, Y.-F. Liu, and D. W. K. Ng, "Energy-Efficient Beamforming Design for Integrated Sensing and Communications Systems," *IEEE Transactions on Communications*, pp. 1–1, 2024.
- [38] F. Xia, Z. Fei, X. Wang, P. Liu, J. Guo, and Q. Wu, "Joint Waveform and Reflection Design for Sensing-Assisted Secure RIS-Based Backscatter Communication," *IEEE Wireless Communications Letters*, vol. 13, no. 5, pp. 1523–1527, 2024.
- [39] K. Zhong, J. Hu, J. Liu, D. An, C. Pan, K. C. Teh, X. Yu, and H. Li, "P2C2M: Parallel Product Complex Circle Manifold for RIS-Aided ISAC Waveform Design," *IEEE Transactions on Cognitive Communications and Networking*, pp. 1–1, 2024.
- [40] Z. Wang, X. Mu, and Y. Liu, "STARS Enabled Integrated Sensing and Communications," *IEEE Transactions on Wireless Communications*, vol. 22, no. 10, pp. 6750–6765, 2023.
- [41] A. Bazzi and M. Chafii, "On Integrated Sensing and Communication Waveforms with Tunable PAPR," *IEEE Transactions on Wireless Communications*, pp. 1–1, 2023.
- [42] S. K. Mohammed and E. G. Larsson, "Per-Antenna Constant Envelope Precoding for Large Multi-User MIMO Systems," *IEEE Transactions on Communications*, vol. 61, no. 3, pp. 1059–1071, 2013.
- [43] F. Liu, L. Zhou, C. Masouros, A. Li, W. Luo, and A. Petropulu, "Toward Dual-functional Radar-Communication Systems: Optimal Waveform Design," *IEEE Transactions on Signal Processing*, vol. 66, no. 16, pp. 4264–4279, 2018.
- [44] O. Aldayel, V. Monga, and M. Rangaswamy, "Successive QCQP Refinement for MIMO Radar Waveform Design Under Practical Constraints," *IEEE Transactions on Signal Processing*, vol. 64, no. 14, pp. 3760–3774, 2016.
- [45] M. Maleki, H. R. Bahrami, and A. Alizadeh, "On MRC-Based Detection of Spatial Modulation," *IEEE Transactions on Wireless Communications*, vol. 15, no. 4, pp. 3019–3029, 2016.
- [46] J.-H. Choi and H.-G. Ryu, "A QAPM(Quadrature Amplitude Position Modulation) for low power consumption communication," in *International Symposium on Wireless and Pervasive Computing*, 2011, pp. 1–4.